

Competing orders in a frustrated Heisenberg model on the Fisher lattice

Atanu Maity,^{1,2,*} Yasir Iqbal,^{3,†} and Saptarshi Mandal^{1,2,‡}

¹*Institute of Physics, Bhubaneswar 751005, Odisha, India*

²*Homi Bhabha National Institute, Mumbai 400 094, Maharashtra, India*

³*Department of Physics, Indian Institute Of Technology Madras, Chennai 600036, Tamil Nadu, India*

(Dated: November 28, 2021)

We investigate the Heisenberg model on a decorated square (Fisher) lattice in the presence of first neighbor J_1 , second neighbor J_2 , and third neighbor J_3 exchange couplings, with antiferromagnetic J_1 . The classical ground state phase diagram in the J_2 - J_3 plane obtained within a Luttinger-Tisza framework is spanned by two antiferromagnetically ordered phases, and an infinitely degenerate antiferromagnetic chain phase. We find that an order-by-disorder transition driven by thermal as well as quantum fluctuations occurs in the chain phase. Interestingly, the spin wave spectrum of the Néel state displays three Dirac nodal loops out of which two are symmetry protected while for the antiferromagnetic chain phase we find symmetry protected Dirac lines. Furthermore, we investigate the spin $S = 1/2$ limit employing a bond operator formalism which captures the singlet-triplet dynamics, and find a rich ground state phase diagram host to variety of valence-bond solid orders in addition to antiferromagnetically ordered phases.

I. INTRODUCTION

In Mott-Hubbard insulators, a reasonable description of the localized electron state at low-temperatures is provided for by the Heisenberg spin Hamiltonian [1]. In the presence of frustrated interactions, which could be geometric or parametric in origin, the determination of the ground state and low-energy physics of the Heisenberg model poses itself as a highly nontrivial problem. The principal motivation in the investigation of frustrated spin systems lies in the lure of finding either magnetically ordered ground states with intricate spin textures or highly correlated nonmagnetic phases such as spin liquids [2–6]. To this end, transition metal oxides have attracted much attention as they are found in nature with a rich diversity of geometrically frustrated lattice structures and thus display a wide spectrum of magnetic behaviors [7, 8]. In particular, in one such family of manganese oxide compounds (MnO_2) such as $\text{K}_{1.5}(\text{H}_3\text{O})_x\text{Mn}_8\text{O}_{16}$, $\text{Ba}_{1.2}\text{Mn}_8\text{O}_{16}$, and $\alpha\text{-MnO}_2$ [9–11], the Mn ions reside on the vertices of a geometrically frustrated network, namely, the hollandite lattice [9, 12, 13]. Experimental studies on these systems have unveiled the presence of a plethora of magnetic phases upon variation of temperature, magnetic field, and doping, which include, an antiferromagnetic state [14], a ferromagnet, helimagnetic order [15, 16], and spin glass behavior.

In order to understand the origin of this diversity in magnetic behaviors it is helpful to disentangle the effects of magnetic frustration from those arising due to the presence of impurities. Recently, theoretical studies employing an Ising model on the hollandite lattice [17, 18] successfully explained the origin of the antiferromagnetic ground state in the disorder free system [19] as

well as the doping-induced transition into a spin-glass state [20–22]. However, the Ising model studied in Ref. [17] cannot account for helimagnetic (and in general noncollinear) orders observed in $\text{K}_{1.5}(\text{H}_3\text{O})_x\text{Mn}_8\text{O}_{16}$ and $\text{K}_{0.15}\text{MnO}_2$ at low temperatures [15, 16]. Experimental investigations on Manganese compounds [23–25] have provided evidence that these systems have small magnetic anisotropies and thus be well described by a Heisenberg model. The zero temperature ($T = 0$) classical magnetic phase diagram of the Heisenberg model on the Hollandite lattice allowing for different signs and strengths of nearest-neighbor couplings was studied in Ref. [26].

The hollandite lattice can be viewed either as coupled two-dimensional triangular lattices stacked in the z -direction or as decorated square lattices (called Fisher lattice) stacked in the y -direction [26]. An understanding of the magnetic Hamiltonian on a lattice which is a two-dimensional projection of the original three-dimensional lattice often provides valuable insights into how magnetic order develops in the original three-dimensional model, and helps flesh out the structure of the (often intricate) spin configurations. In this regard, investigation of the magnetic phases in kagome lattice as an insightful route towards understand the complex magnetism in the pyrochlore lattice is noteworthy [27]. Herein, we adopt the route of understanding the magnetism of the Hollandite lattice by viewing it as coupled Fisher lattices since the non-trivial mechanism of magnetic order in $\alpha\text{-MnO}_2$ materials seems to arise due to the coupling in y -direction [13, 18, 26, 28]. In this work, we carry out a detailed analysis of the magnetic phases present in the $T = 0$ classical phase diagram and investigate fluctuation effects beyond the classical limit via a spin-wave analysis and a bond-operator formalism for spin $S = 1/2$.

We consider a minimal model on the Fisher lattice [see Fig. 1] such that J_1 couples connects the vertices of neighboring squares, J_2 defines the nearest-neighbour coupling within the squares, and J_3 is the second nearest-neighbor

* atanu.maity@iopb.res.in

† yiqbal@physics.iitm.ac.in

‡ saptarshi@iopb.res.in

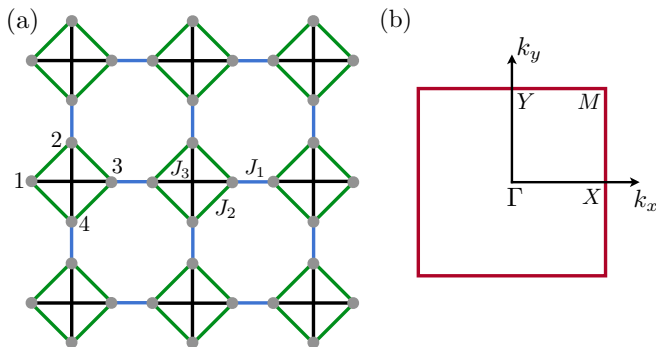


FIG. 1. (a) The Fisher lattice showing the three exchange couplings J_1 (blue) connecting sites on octagons, J_2 (green) connecting the sites of a square, and J_3 (black) connecting the diagonals of a square, of Eq. (1), with the four sites of the unit cell marked by 1, 2, 3, and 4. (b) The first Brillouin zone of the Fisher lattice with the high-symmetry points marked.

(diagonal) coupling within each square. The inclusion of a J_3 coupling has been motivated from recent studies [13, 28] which suggest that it might be necessary to describe the magnetism in Hollandite systems. At the classical level, a Luttinger-Tisza analysis [29–31] of the (J_1, J_2, J_3) parameter space reveals the presence of different kinds of antiferromagnetically (AF) ordered states, an infinitely degenerate uncorrelated AFM chain phase, as well a topological phase with gapless surface magnon states, depending on the sign and strength of the couplings. Furthermore, we investigate the role of quantum and thermal fluctuations on these ground states and find that fluctuations drive an order-by-disorder transition in the uncorrelated AFM chain phase. We complement our study by going beyond the spin-wave approximation and compute the relative stability of the semi-classical ground state within a variational ansatz by comparing the energies of competing states and find that each of them is stable as they have a finite triplon excitation gap over suitable singlet states.

Our plan of presentation is as follows. In Sec. II, we define the model Hamiltonian and the Luttinger-Tisza framework employed to obtain the classical phase diagram. In section III A, we describe the $T = 0$ classical ground states and study the effect of thermal fluctuations using a classical Monte Carlo method. In Sec. IV and Sec. V, we study the impact of quantum and thermal fluctuations to harmonic order on the ground states, respectively. In Sec. VI, we analyse our model Hamiltonian for spin $S = 1/2$ within the scope of a bond operator formalism and show the existence of three different types of quantum paramagnetic ground states, namely, a plaquette VBS, and two other dimer ordered states. Finally, we summarize and discuss our results in Sec. VII.

II. MODEL AND METHODS

We consider a two-dimensional plane of the Hollandite lattice [see Fig. 1], called the decorated square (Fisher) lattice, which is characterized by a four-site geometrical unit cell [32]. The interactions between the spins localized on the vertices of this lattice are governed by a Heisenberg Hamiltonian

$$\hat{\mathcal{H}} = J_1 \sum_{\langle i,j \rangle_1} \hat{\mathbf{S}}_i \cdot \hat{\mathbf{S}}_j + J_2 \sum_{\langle i,j \rangle_2} \hat{\mathbf{S}}_i \cdot \hat{\mathbf{S}}_j + J_3 \sum_{\langle i,j \rangle_3} \hat{\mathbf{S}}_i \cdot \hat{\mathbf{S}}_j, \quad (1)$$

where the J_1 , J_2 , and J_3 superexchange couplings are schematically illustrated in Fig. 1(a). It is worth noting that earlier studies [17, 26] investigating the magnetism of the full three-dimensional Hollandite lattice, the consideration of in-plane interactions was restricted to inter-square (J_1) and nearest-neighbor intra-square (J_2) couplings only [33], while the inter-plane coupling was found to yield helimagnetic order. Recent experimental studies [13, 28] on Hollandite compounds have pointed to relatively more intricate ground states compared to those found in Refs. [15–17, 26]. In particular, in Ref. [28], the in-plane magnetic ground state was found to possess a magnetic unit cell which is a 4×4 expansion of the geometrical unit cell. Though the materials in question potentially involve more complex charge orderings which are likely to induce to further magnetic coupling between the Mn atoms, it is understood that a simple model which accounts for only the above two mentioned in-plane interactions (J_1 and J_2 in Fig. 1(a)) is not sufficient to explain the formation of a magnetic order with a 4×4 expanded magnetic unit cell. The above fact motivates us to explore a larger parameter space of exchange couplings, and to this end, we propose the simplest extension by introducing an additional second nearest-neighbor (diagonal) coupling within each square, i.e., J_3 in Fig. 1(a). In our study we consider all possible signs and strengths of the (J_1, J_2, J_3) couplings.

Our analysis of the ground states of the classical version of Eq. (1) employs the Luttinger-Tisza method. The corresponding classical model is obtained by normalizing the spin operators with respect to their angular momentum S and taking the limit $S \rightarrow \infty$ [34, 35]. Consequently, the spin operators in Eq. (1) are replaced by ordinary vectors of unit length at each lattice site i . For a generic spin interaction, we have the following classical Hamiltonian that needs to be minimized

$$\mathcal{H} = \sum_{i,j,\alpha,\beta} J_{\alpha\beta}(\mathbf{R}_{ij}) \mathbf{S}_{i,\alpha} \cdot \mathbf{S}_{j,\beta}, \quad (2)$$

where i, j denotes the corresponding Bravais lattice sites separated by lattice translation vectors \mathbf{R}_{ij} and α, β indices denote the sublattice sites. The underlying Bravais lattice of the Fisher lattice is the square lattice. The Luttinger-Tisza method [29–31] seeks to find a ground state of Eq. (2) by enforcing the spin-length constraint

at a global level, i.e., $\sum_i |\mathbf{S}_i^z| = S^2 n$, where n is the total number of lattice sites, a condition termed as the *weak constraint*. This constraint amounts to permitting site-dependent average local moments which take us beyond the classical limit by approximately incorporating some aspects of quantum fluctuations [36].

A solution of this relaxed problem is achieved by decomposing the spin configuration into its Fourier modes $\tilde{\mathbf{S}}_\alpha(\mathbf{k})$ on the four sublattices of the Fisher lattice

$$\mathbf{S}_{i,\alpha} = \frac{1}{\sqrt{N/4}} \sum_{\mathbf{k}} \tilde{\mathbf{S}}_\alpha(\mathbf{k}) e^{i\mathbf{k}\cdot\mathbf{r}_{i,\alpha}}. \quad (3)$$

Inserting this equation into Eq. (2) results in

$$\mathcal{H} = \sum_{\mathbf{k}} \sum_{\alpha,\beta} \tilde{J}_{\alpha\beta}(\mathbf{k}) \tilde{\mathbf{S}}_\alpha(\mathbf{k}) \cdot \tilde{\mathbf{S}}_\beta(-\mathbf{k}), \quad (4)$$

with the interaction matrix given by

$$\tilde{J}_{\alpha\beta}(\mathbf{k}) = \sum_{i,j} J_{\alpha\beta}(\mathbf{R}_{ij}) e^{i\mathbf{k}\cdot\mathbf{R}_{ij}}. \quad (5)$$

$$\begin{pmatrix} 0 & J_2 e^{i(k_x - k_y)a} & J_3 e^{i2k_x a} + J_1 e^{ik_x b} & J_2 e^{i(k_x + k_y)a} \\ J_2 e^{-i(k_x - k_y)a} & 0 & J_2 e^{i(k_x + k_y)a} & J_3 e^{i2k_x a} + J_1 e^{ik_x b} \\ J_3 e^{-i2k_x a} + J_1 e^{-ik_x b} & J_2 e^{-i(k_x + k_y)a} & 0 & J_2 e^{i(k_x - k_y)a} \\ J_2 e^{-i(k_x + k_y)a} & J_3 e^{-i2k_x a} + J_1 e^{-ik_x b} & J_2 e^{-i(k_x - k_y)a} & 0 \end{pmatrix}$$

In the region of parameter space defined by $J_3 > |J_2|$, we find that the minimal eigenvalue wave vector $(k_x, k_y)_0$ is given by

$$\begin{aligned} (k_x, k_y)_0 &= (2m\pi/3, k_y) & \text{or} \\ (k_x, k_y)_0 &= (k_x, 2n\pi/3) \end{aligned} \quad (6)$$

where $m, n \in \mathbb{Z}$, hence, indicating long-range ordering in one direction with an absence of relative ordering in the other direction. Along the line $J_2 = J_3$, we find

$$(k_x, k_y)_0 = (k_x, k_y), \quad (7)$$

pointing to a degenerate ground state manifold. In the remaining regions of parameter space we find

$$(k_x, k_y)_0 = ((2n+1)\pi/3, (2m+1)\pi/3), \quad (8)$$

thus pointing towards long range ordering with commensurate ordering wave vectors. The absence of an incommensurate ordering wave vector implies that degree to which mutual interactions between spins is satisfied is likely to be determined locally, and hence, as a starting point it is helpful to pursue an energy minimization of a local cluster of spins. To this end, we employ a variational approach which proceeds by first constructing spin configurations of a local cluster of spins that minimize its energy and subsequently attempt to construct a global

The modes which respect the weak constraint are given by the wave vector \mathbf{k} , for which the *lowest* eigenvalue of Eq. (5) has its minimum. The eigenvector corresponding to this eigenvalue gives the relative weight of the modes on the sublattices [37], which means that these modes do not fulfill the strong constraint ($|\mathbf{S}_i^z| = S^2$, i.e., fixed spin-length constraint on every site) if the components of the eigenvector do not have the same magnitude. On the other hand, if this condition is met, the true ground state of the classical model is a coplanar spiral determined by the optimal Luttinger-Tisza wave vector [38].

III. CLASSICAL GROUND STATES

A. Luttinger-Tisza analysis

The interaction matrix $\tilde{J}_{\alpha\beta}(\mathbf{k})$ for our model takes the form

spin configuration which also satisfies the local minimum energy configuration of the cluster of spins. We verify the accuracy of our global spin configurations from classical Monte Carlo simulations.

To start with, we consider a cluster of four spins that constitute a unit cell of the Fisher lattice. The spin configuration is parameterized by observing that the lattice can be described by a collection of horizontal and vertical connections which are coupled via J_2 bonds. Each horizontal and vertical string of connections hosts two sublattices each. The angle between the spins within both the sublattices are assigned an angle γ , while the angle between the spins belonging to the same sublattice but in different chains is assigned an angle α . This choice of ansatz gives an energy density

$$\begin{aligned} E/NS^2 &= \frac{1}{4} (J_1 (\cos(\gamma - k_x) + \cos(\gamma - k_y)) + J_2 (2 \cos \alpha \\ &\quad + \cos(\alpha + \gamma) + \cos(\alpha - \gamma)) + 2J_3 \cos \gamma). \end{aligned} \quad (9)$$

The above expression has four free parameters which need to be determined to obtain the ground state spin configuration. We note that since the antiferromagnetic J_1 bond is not frustrated by any other interaction, one may put forth an ansatz in which the spins connected by the J_1 bond will be antiparallel, i.e., $k_x - \gamma = k_y - \gamma = \pi$, and Eq. (9) simplifies to

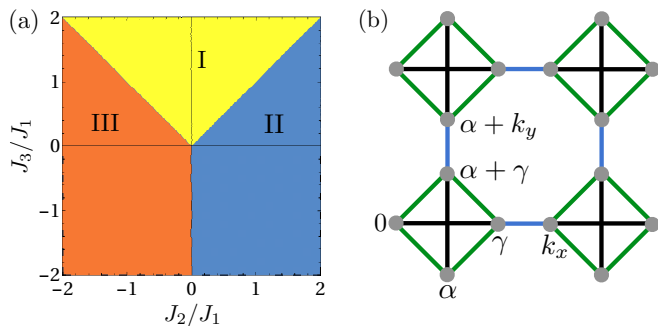


FIG. 2. (a) Classical phase diagram of J_1 - J_2 - J_3 Heisenberg model on the Fisher lattice with the couplings as defined in Fig. 1(a) and Eq. (1), (b) parameterization of a generic spin configuration with $\gamma = k_x + \pi$ and $k_x = k_y = k$.

$$E/NS^2 = \frac{1}{2}(J_2 \cos \alpha(1 - \cos k_x) - J_3 \cos k_x - J_1). \quad (10)$$

Upon minimizing Eq. (10) with respect to k_x and α we get the following two sets of conditions for a spin configuration to qualify as a ground state

$$\sin k_x(J_2 \cos \alpha + J_3) = 0 \quad (11)$$

$$\sin \alpha(1 - \cos k_x) = 0. \quad (12)$$

The solutions (k_x, α) satisfying the conditions [Eqs. (11) and (12)] corresponding to different phases are described below

1. Antiferromagnetic chain phase

This phase is characterized by $(k, \alpha) = (0, \alpha)$ and is stabilized for $J_3 \geq |J_2|$. It is depicted as phase I (yellow region) in the phase diagram shown in Fig. 2(a). It features perfect antiferromagnetic order along either the horizontal or vertical chains, however, there is a complete absence of spin correlations between any two of these ordered chains [see Fig. 3(a)]. This implies that within any given four site unit cell, the spins coupled by J_3 bonds are antiferromagnetically aligned while there is no correlation between the spins connected by J_2 bonds, and hence, the angle α can take any value implying an infinite degeneracy of the ground state manifold. The ground state energy is then independent of α

$$E/NS^2 = -\frac{1}{2}(J_3 + J_1). \quad (13)$$

In the above expression, the independence of the energy on α arises due to a cancellation of the contributions from two bonds connected by J_2 within a given square plaquette. The existence of such a degeneracy within each square together with long range antiferromagnetic order along horizontal or vertical chains poses itself as an interesting scenario. In Secs. IV and V, we investigate the effects of thermal and quantum fluctuations in lifting this degeneracy.

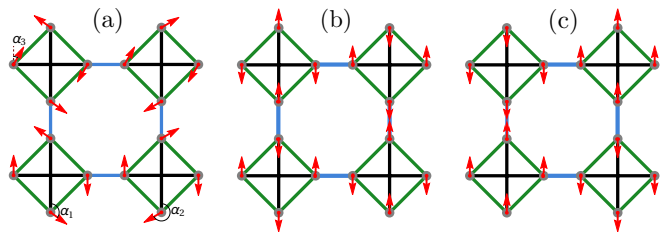


FIG. 3. Spin configuration in (a) phase-I (uncorrelated AFM chain) with $(k, \alpha) = (0, \alpha)$. The individual horizontal or vertical chains have perfect AFM order, the relative orientations between them is not fixed. With respect to lower horizontal chain the orientations of the two vertical chains is α_1 and α_2 , respectively. Also, note that the orientation of upper horizontal chain with respect to lower horizontal chain is α_3 , i.e., the system has an infinite degeneracy, (b) phase-II (Néel phase) with $(k, \alpha) = (\pi, \pi)$, and (c) phase-III (sublattice Néel phase) with $(k, \alpha) = (\pi, 0)$.

2. Néel phase

For $J_3 < |J_2|$, we enter a region of parameter space where the arbitrariness in the choice of the parameter α in the uncorrelated antiferromagnetic chain phase gets lifted. In particular, for $J_2 > 0$ and $J_3 < J_2$, we obtain a Néel ordered phase [marked as phase II (blue region) in Fig. 2(a)]. This phase is characterized by $(k, \alpha) = (\pi, \pi)$ which signifies that within any given unit cell (square) there is perfect antiferromagnetic order, and that the spins in neighboring unit cells are aligned antiferromagnetically with respect to each other [see Fig. 3(b)]. However, unlike the familiar Néel phase on the square or honeycomb lattice, not all antiferromagnetic bonds are satisfied when $J_3 > 0$, as the spins connected by the J_3 couplings remain frustrated. The ground state energy of this phase is given by,

$$E/NS^2 = -\frac{1}{2}(2J_2 - J_3 + J_1). \quad (14)$$

Upon entering the region $J_3 < 0$, this phase is further stabilized since the spins coupled via J_3 bonds are ferromagnetically aligned in this Néel phase.

3. Sublattice Néel phase

In the region $J_2 < 0$, when $J_3 < |J_2|$, the free parameter α characterizing phase I now evaluates to zero implying that all spins within a given unit cell are ferromagnetically aligned. Furthermore, these four-site unit cells form Néel order throughout the lattice, and hence, each sublattice is Néel ordered [see Fig. 3(c)]. This state is thus characterized by $(k, \alpha) = (\pi, 0)$. The ground state energy density can be written as,

$$E = -\frac{1}{2}(2|J_2| - J_3 + J_1). \quad (15)$$

When $J_3 < 0$, the spin configuration satisfies all the couplings.

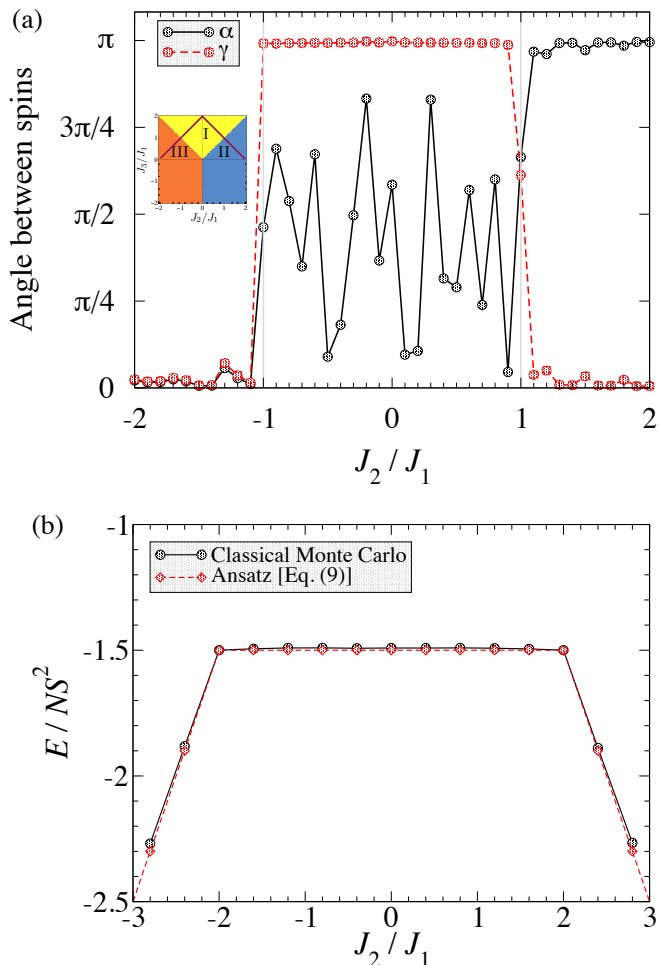


FIG. 4. From classical Monte Carlo simulations, (a) variation of the angles α and γ [see Fig. 2(b)] parameterizing the spin configurations [Eq. (9)] along the cut $|J_2| + J_3 = 2$ (marked by a maroon line within the phase diagram shown as an inset), (b) The ground state energy per site (in units of J_1) E/NS^2 vs J_2 for fixed $J_3 = 2$.

B. Classical Monte Carlo analysis

Since the Luttinger-Tisza approach is not *a priori* expected to give the exact ground state spin configuration, and given the fact that our approach is based on a variational ansatz [Eq. (9)], we perform classical Monte Carlo simulations to investigate the accuracy of our analysis. We consider a system of 1600 spins ($20 \times 20 \times 4$), and employ parallel tempering which allows us to reach temperatures $T/J_1 S^2 \sim 0.001$. In Fig. 4(a) we show how the angles α and γ [see Fig. 2(b)] parameterizing the spin configuration via ansatz in Eq. (9) vary in parameter space along the cut $|J_2| + J_3 = 2$. It is clearly seen that the spin configurations determined from the (numerically) exact classical Monte Carlo simulations are in complete agreement with those determined from the variational ansatz [Eq. (9)] thus validating the classical phase diagram of Fig. 2(a). In Fig. 4(b), we

plot the ground state energy as obtained from classical Monte Carlo simulations as well as from the variational ansatz of Eq. (9) as a function of J_2 for a fixed value of $J_3 = 2$. It is worth noting that in the region $J_3 > |J_2|$, i.e., phase-I, the ground state energy is independent of J_2 which is a manifestation of the degenerate nature of the ground state in this region.

Having discussed the classical ground states in entire parameter space, it is instructive to calculate the magnetic structure factor which can be experimentally measured in a neutron diffraction experiment [39] to confirm the magnetic ground states discussed before. As described, we have found three different magnetic ground states namely uncorrelated AFM chain phase, Néel phase and sublattice Néel phase depending on the sign and magnitude of the coupling parameter J_i 's. Here, we calculate the structure factor by an unbiased Monte Carlo simulation for three different sets of parameter values representing these three classical ground states. The equal-time (static) spin structure factor that we calculate is defined as

$$S(\mathbf{q}) = \frac{1}{N} \sum_{i,j} e^{-i\mathbf{q} \cdot \mathbf{R}_{ij}} \langle \mathbf{S}_i \cdot \mathbf{S}_j \rangle \quad (16)$$

where N is the total number of sites. In our numerical simulation we have taken the nearest neighbour distance between two sites to be unit length. This implies that the distance between the neighbouring unit cells is of length three units which makes the periodicity of $S(\mathbf{q})$ as $2\pi/3$. In Fig. 5 we show the structure factor in different parameter regime corresponding to different magnetic ground state [see Fig. 2]. We note that the uncorrelated AFM chain phase has no average global ordering in any direction. The perfect AFM order in a given chain yields vanishing contribution when summed over all chain. Hence, we expect merely a featureless structure factor with the presence of subdued peak at the zone boundary (corresponding to ordering vector \mathbf{k} to be zero due to statistical average) as can be seen in Fig. 5(a). For magnetic ground state given by phase-II and phase-III, we note that a global AFM (Néel) order should yield a peak at $\mathbf{k} = (m\frac{\pi}{3}, n\frac{\pi}{3})$ with ' m, n ' being an odd integer. However, the peaks at above mentioned points would be modulated due to the form factor (similar to atomic form factor) of the magnetic ordering in a given unit cell of Néel phase (phase-II) and sublattice Néel phase (phase-III). It can be easily checked that the form factor of the phase-II and phase-III are $(\cos k_x - \cos k_y)$ and $(\cos k_x + \cos k_y)$, respectively. The form factor is zero along the line $k_x = 2m'\pi \pm k_y$ for phase-II and $k_x = (2m' + 1)\pi \pm k_y$ for phase-III where m' is any integer including zero. Thus, the expected peaks at $\mathbf{k} = (m\frac{\pi}{3}, n\frac{\pi}{3})$ will be modulated due to such lines of zero intensity and it would remove some peaks in structure factor which are expected due to global Néel orders. Fig. 5(b) represents the structure factor for the Néel order (phase-II). We see that the peaks are appearing

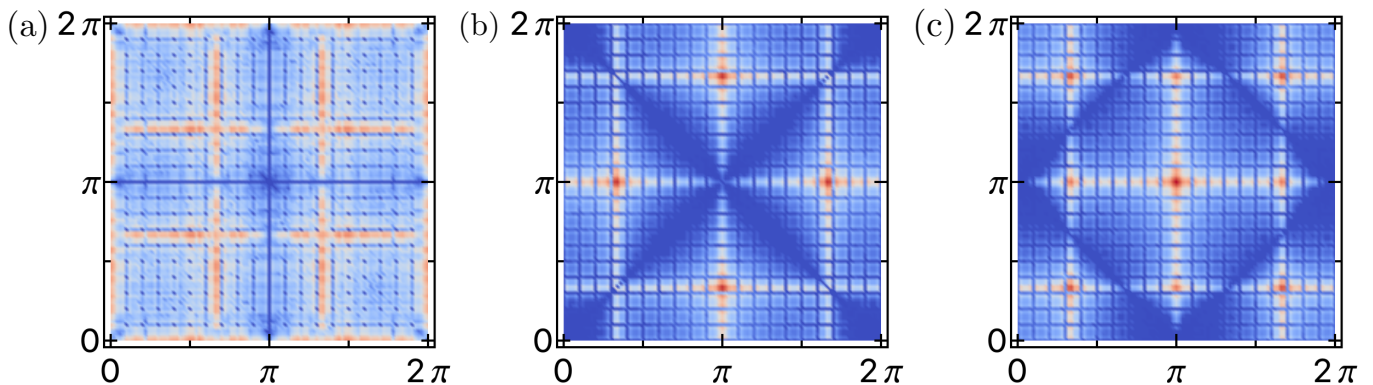


FIG. 5. The static (equal-time) spin structure factor obtained from classical Monte Carlo simulations for the three different phases in the classical phase diagram of Fig. 2(a) evaluated at $T/J_1 S^2 = 0.01$ for a system of 1600 spins, (a) phase-I at $(J_2/J_1, J_3/J_1) = (1, 4)$, (b) phase-II at $(J_2/J_1, J_3/J_1) = (4, 1)$, and (c) phase-III $(J_2/J_1, J_3/J_1) = (-4, 1)$.

at $\mathbf{k} = (m\frac{\pi}{3}, n\frac{\pi}{3})$ with $m \neq n$ due to the modulation coming from form factor mentioned before. On the other hand, such destructive modulation is absent for the sublattice Néel phase and the peaks appear expectedly at $\mathbf{k} = (m\frac{\pi}{3}, n\frac{\pi}{3})$ with ‘ m ’ and ‘ n ’ being odd integer as mentioned. In practice, the particular material may not have the exact symmetry of the lattice we have considered. For example the unit cell may not be a square as taken here and also the distances between different neighbouring sites joined by J_i may also be different and in that case the experimentally obtained structure factor might be different than what is shown in Fig. 5. However the structure factor in that case can be easily compared by evaluating Eq. (16) with modified lattice parameters, mainly the different values of \mathbf{R}_{ij} .

IV. SPIN WAVE ANALYSIS

A. Antiferromagnetic chain phase

The classical antiferromagnetic chain phase [phase-I in Fig. 2(a)] has an infinitely degenerate ground state manifold. In particular, on a lattice consisting of N horizontal and M vertical lines [see Fig. 2(b)], there are $N \times M$ independent α parameters each of which can take on values ranging from 0 to 2π . It is thus natural to ask the question whether quantum fluctuations can lift this degeneracy via an order-by-disorder mechanism [40, 41] and select a unique configuration parameterized by a certain value of α . To investigate the role of quantum fluctuations, we carry out a linear spin wave analysis. To this effect, we rotate our coordinate system in such a way that the z -axis of the local coordinate system coincides with the axis of the local spin orientation,

$$(\hat{S}_i^x, \hat{S}_i^y, \hat{S}_i^z) = R_x(\pi/2)R_z(\phi_i)(\hat{S}_i^{x'}, \hat{S}_i^{y'}, \hat{S}_i^{z'}). \quad (17)$$

The Holstein-Primakoff [42] transformation can now be written as

$$\begin{aligned} \hat{S}_{i,m}^{z'} &= s - \hat{a}_{i,m}^\dagger \hat{a}_{i,m} \\ \hat{S}_{i,m}^{x'} &= \sqrt{\frac{s}{2}} (\hat{a}_{i,m}^\dagger + \hat{a}_{i,m}) \\ \hat{S}_{i,m}^{y'} &= i\sqrt{\frac{s}{2}} (\hat{a}_{i,m}^\dagger - \hat{a}_{i,m}). \end{aligned} \quad (18)$$

Within a quadratic approximation to the boson operators we find that a uniform choice of α (when all $N \times M$ values of α are the same) is energetically favorable compared to disordered configurations of α (when all $N \times M$ values of α are different), indicating an order-by-disorder mechanism at work. The lifting of the degeneracy is only *partial* as α (which is now the same for all $N \times M$ sites) can still take on any value between 0 and 2π yielding the same ground state energy, and the hence there still remain an infinite number of degenerate ground states. However, the magnon spectrum for each value of α need not be the same and thus we investigate the α dependence of the spin-wave spectrum. In Appendix A we provide the expressions of the resulting Hamiltonian after implementing the Holstein-Primakoff transformation corresponding to Eqs. (17) and (18). As expected, the Hamiltonian is invariant under \mathcal{PT} -symmetry which is defined as $\mathcal{PT} = \sigma_x \otimes \sigma_0 \mathcal{K}$ (where \mathcal{K} is the complex conjugation operator). In phase-I, the magnetic and crystallographic unit cells are identical, as a result of which we get a 8×8 Hamiltonian matrix [see Eq. (A1)] in k -space. As a consequence of \mathcal{PT} symmetry we obtain four doubly-degenerate magnon branches as shown in Fig. 6 with the following dispersion relations,

$$\epsilon(k)_{1,2} = \frac{1}{2} \sqrt{p_k \pm \frac{1}{2} \sqrt{Q(0)f_k + g_k(0) + h_k}} \quad (19)$$

$$\epsilon(k)_{3,4} = \frac{1}{2} \sqrt{p_k \pm \frac{1}{2} \sqrt{Q(\alpha)f_k + g_k(\alpha) + h_k}} \quad (20)$$

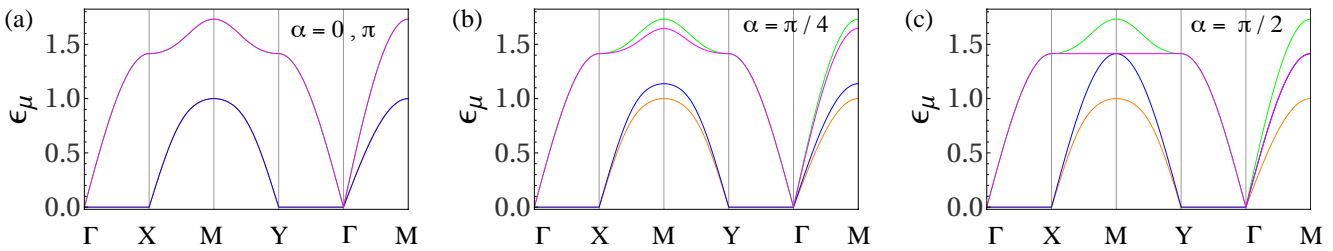


FIG. 6. Free magnon spectrum corresponding to Eq. (19) and Eq. (20) in phase-I for the parameter values $(J_2/J_1, J_3/J_1) = (1, 2)$ plotted along the high-symmetry path $\Gamma(0, 0)$, $X(\pi, 0)$, $M(\pi, \pi)$, and $Y(0, \pi)$.

where $Q(\alpha) = \frac{2(J_2)^2 \cos^2 \alpha - (J_3)^2}{4}$ and

$$p_k = \frac{J_3}{4}(2 - \cos k_x - \cos k_y) \quad (21)$$

$$f_k = (\cos(k_x + k_y) + \cos(k_x - k_y)) \quad (22)$$

$$g_k(\alpha) = (J_2)^2 \cos^2 \alpha (1 - \cos k_x - \cos k_y) \quad (23)$$

$$h_k = (J_3)^2 (2 + \cos(2k_x) + \cos(2k_y))/8 \quad (24)$$

From Eq. (19) we see that there are two modes which are independent of α , and Eq. (20) shows that the other two modes are α dependent. For any given value of α there are two Goldstone modes originating from the spontaneously broken $U(1)$ symmetry, and we observe the presence of zero-energy modes along the segment $\overline{\Gamma X}$ and $\overline{\Gamma Y}$. The presence of the zero-energy modes can be understood from Eqs. (19) and (20) which upon substituting $k_x(k_y) = 0$ and $k_y(k_x) = k$ give, in the large wavelength limit, $\epsilon_\mu \approx ck$, which is the excitation energy of an antiferromagnetic chain, and where $c = \sqrt{J_3}/8$ for the first set of modes [Eq. (19)] and $c = \sqrt{3J_3}/8$ for the second set of modes [Eq. (20)]. It is worth noting that along the $k_x = 0$ and $k_y = 0$ axis we have linear band crossings along the line segments $\overline{\Gamma X}$ and $\overline{\Gamma Y}$ in the Brillouin zone, thus forming Dirac nodal lines. We now discuss how the spin wave spectrum depends on α . (i) For $\alpha = 0$ or π : In this case the system has a two sublattice Néel order. The Hamiltonian in this case is block diagonal [see Appendix A], and each block is \mathcal{PT} invariant which gives rise to two 4-fold degenerate bands [see Fig. 6(a)]. (ii) For $\alpha = \pi/4$: The block diagonal structure disappears and as a result the two 4-fold degenerate bands split into four 2-fold degenerate bands [see Fig. 6(b)]. (iii) For $\alpha = \pi/2$: In this case we have a band touching of the α dependent bands at the M point which is a consequence of the underlying mirror reflection symmetry about the k_x, k_y and $k_x = k_y$ axes. We note that there is a Dirac nodal line along the segment $\overline{\Gamma M}$ [see Fig. 6(c)].

B. Phase-II and Phase-III

This phase has a perfect antiferromagnetic structure which is the same as for the unfrustrated case ($J_3 = 0$ and $J_1, J_2 > 0$) studied in Ref. [43] where the presence of two Dirac nodal loops was found. The magnetic unit

cell (8-sites) is twice the size of the crystallographic unit cell (4 sites). In the bipartite representation, the Hamiltonian can be written as in Eq. (A5), and is seen to be block diagonal with each block being \mathcal{PT} invariant. This results in four 4-fold degenerate bands shown in Fig. 7. Similar to what was found for the unfrustrated model ($J_3 = 0$), we find two nodal loops [marked by blue line in Fig. 8(a)], namely, in Figs. 7(a) and 7(f) we see that the black circled points form one nodal loop while the cyan circled points form the second nodal loop. In the absence of a J_3 coupling it was shown in Ref. [43] that the Dirac nodal loops are topologically protected, and that there is a triple band touching at the Γ and M points, while in the presence of additional J_3 coupling we find a quadruple band touching at the X and Y points as shown in Fig. 7(a). Furthermore, we find that a J_3 coupling, leads to the appearance of an additional Dirac nodal loop along the Brillouin zone boundary and also along the $k_x(k_y) = 0$ axes [see Fig. 7(d)] and marked by an orange segments in Fig. 8(a)]. However, this additional loop appears only for particular choices of parameters shown in Fig. 8(b), and is not protected by any symmetry except at the time-reversal invariant momentum points, i.e., the Γ and M points [see Fig. 7(f) and Fig. 7(i)], where there remains a two-fold degeneracy since the Hamiltonian given by Eq. (A5) is invariant under $\mathcal{T} = i\sigma_y \mathcal{K}$ operator.

In phase-III, whose magnetic structure has an eight site unit cell, we similarly find that the Hamiltonian Eq. (A8) is block diagonal with each block being \mathcal{PT} invariant, leading to four-fold degenerate bands. However, the symmetry protected Dirac nodal loops of phase-II are not found in phase-III, on the other hand, the additional nodal loop along the zone boundary and $k_x(k_y) = 0$ axis found for phase-II also appear in phase-III for the same choice of parameters shown in Fig. 8(b).

V. THERMAL AND QUANTUM ORDER-BY-DISORDER EFFECTS

In phase-I, at zero temperature any value of $\alpha \in (0, 2\pi)$ is a valid ground state. However, at finite temperature, the fluctuation of the spins explicitly contribute to the α dependent free energy. This leads to a lifting of the degeneracy in the parameter α , via a thermal order-by-disorder mechanism [44–46]. To this effect, we introduce

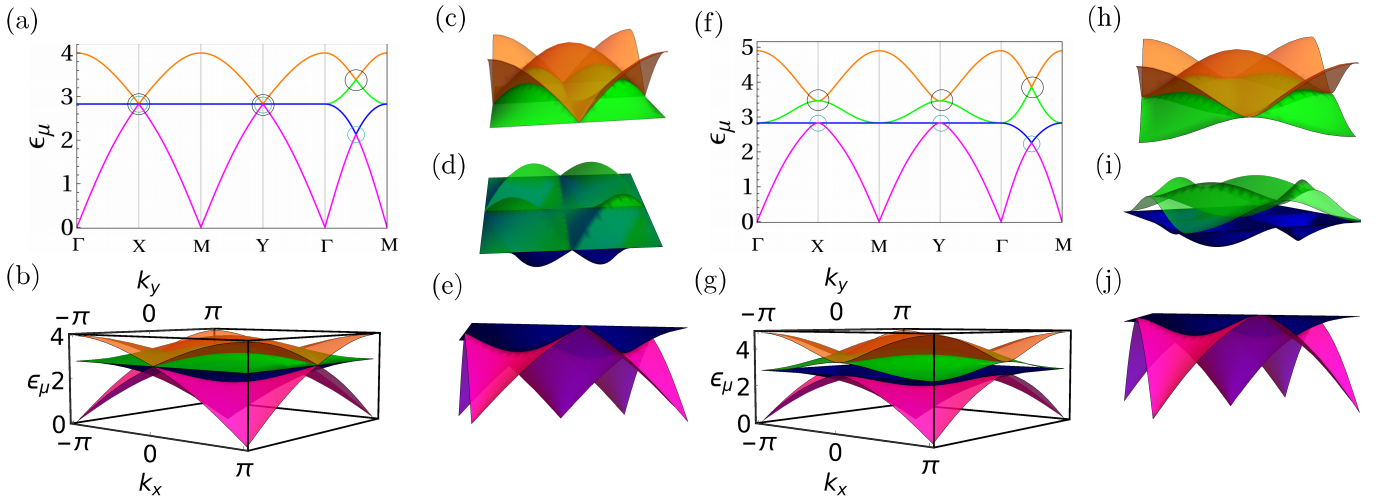


FIG. 7. Free magnon spectrum for phase-II (Néel phase): (a), (b) $(J_2, J_3) = (2, 1)$ and (f), (g) $(J_2, J_3) = (3, 2)$, (c), (d), (e) and (h), (i), (j) represent the band touchings between different bands, which form the Dirac nodal loops for the two above-mentioned choices of parameters, respectively. Notice that the nodal loop due to touchings of the bands denoted by green and blue colors appears for some choices of parameters and gaped out for other choices. Hence, this nodal loop is not protected by any symmetry whereas the nodal loops due to touchings of upper and lower two bands survive for all choices of parameters, thereby rendering these loops symmetry protected.

a spin deviation $\theta_{\mathbf{R},\mu} \rightarrow \theta_{\mathbf{R},\mu}^0 + \delta\theta_{\mathbf{R},\mu}$, where $\theta_{\mathbf{R},\mu}$ is the ground state spin configuration of the μ^{th} sublattice of a unit cell with radius vector \mathbf{R} and $\delta\theta_{\mathbf{R},\mu}$ is the deviation from ground state spin configuration. Substituting this in Eq. (1) and expanding around the ground state up to quadratic order in $\delta\theta_{\mathbf{R},\mu}$, in Fourier space we obtained, $\hat{\mathcal{H}} = E_{\text{GS}} + \hat{\mathcal{H}}_{\text{fluctuation}}$ with

$$\hat{\mathcal{H}}_{\text{fluctuation}} = \sum_{\mathbf{q}} \psi_{\mathbf{q}}^\dagger A_{\mathbf{q}}(\alpha) \psi_{\mathbf{q}} \quad (25)$$

where $\psi_{\mathbf{q}} = [\delta\theta_{\mathbf{q},1} \ \delta\theta_{\mathbf{q},2} \ \delta\theta_{\mathbf{q},3} \ \delta\theta_{\mathbf{q},4}]^T$, and E_{GS} is the ground state energy.

In this (harmonic) approximation, the fluctuations can be integrated out in the partition sum, and give rise to a linear- T dependence in the free energy $\mathcal{F}(\alpha, T)$. Follow-

ing Ref. [46], $\mathcal{F}(\alpha, T)$ can be written as

$$\mathcal{F}(\alpha, T) = E_{\text{GS}} - NT \ln T + T \sum_{\mathbf{q} \in \text{BZ}} \ln(\det A_{\mathbf{q}}(\alpha)), \quad (26)$$

where the last term is the α dependent part of the low-temperature entropy density. The state which minimizes this term corresponds to the minimum of the free energy—this is the entropic order-by-disorder selection mechanism discussed in Refs. [40, 41, 45, 46]. Furthermore, the energy of the spin-wave modes is $\hbar S \epsilon_{\mathbf{q},\mu}(\alpha)$ in the semi-classical description for spins of length $S \gg 1$. Quantum fluctuations then choose the state with the lowest zero-point energy

$$\mathcal{E}_{\text{ZP}}(\alpha) = \sum_{\mathbf{q} \in \text{BZ}} \frac{\hbar S}{2} \epsilon_{\mathbf{q},\mu}(\alpha). \quad (27)$$

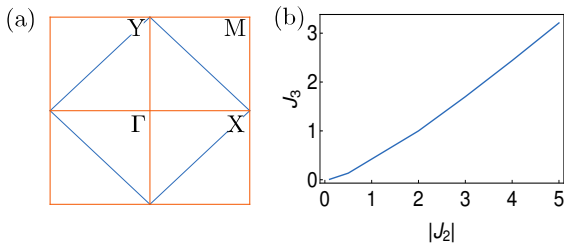


FIG. 8. (a) Projection of Dirac nodal loop on the first Brillouin zone. The blue line denotes the symmetry protected nodal loops whereas the orange one appears for some specific choices of parameters. (b) denotes the choices of parameters where the additional nodal loop appears which is not protected by any symmetry.

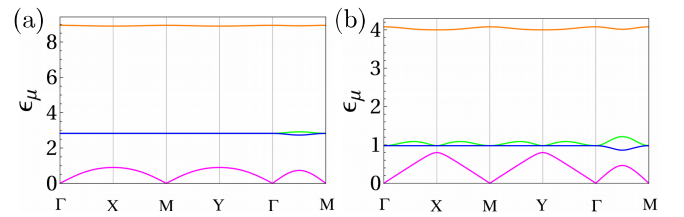


FIG. 9. Free magnon spectrum for phase-III (sublattice Néel phase) for (a) $(J_2, J_3) = (-2, 1)$ and (b) $(J_2, J_3) = (-0.8, 0.6)$. Unlike Néel phase there is no robust Dirac nodal loop in this phase. However similar to Néel phase in some choices of parameters a nodal loop (not protected by any symmetry) appears along the zone boundary and $k_x = 0$ and $k_y = 0$ axes as can be seen from figure (a).

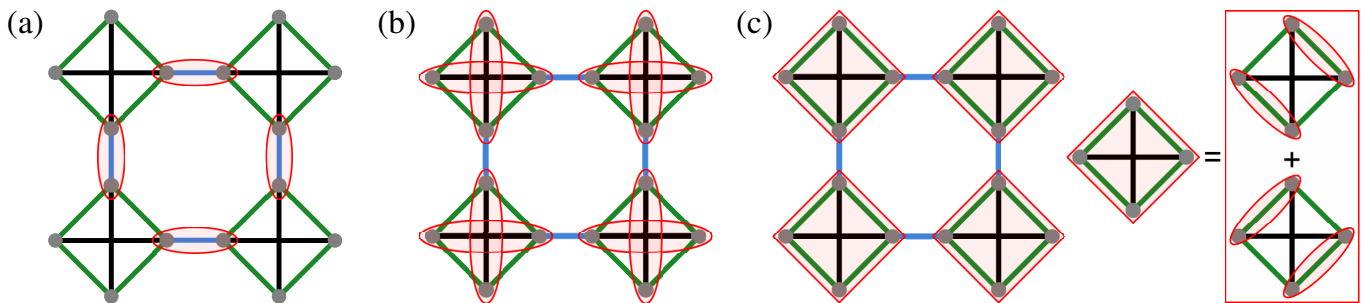


FIG. 10. A schematic illustration of the pattern of singlet dimer formations for the parameter regimes of Eq. (1), (a) $|J_1| \gg (|J_2|, |J_3|)$ (VBS₁), (b) $|J_3| \gg (|J_1|, |J_2|)$ (VBS₂), (c) $|J_2| \gg (|J_1|, |J_3|)$ (Plaquette RVB) wherein the quantum ground state is given by a superposition of two states with dimer formation on the opposite sides of the square as shown in the right panel.

The $\mathcal{E}_{\text{ZP}}(\mathbf{Q})$ behaves qualitatively like the the last term of Eq. (26) and selects the same ordering vectors. In the region of the phase diagram occupied by phase-I, we find that thermal and quantum fluctuations select a value of α equal to 0 or π .

VI. BOND OPERATOR ANALYSIS: VALENCE BOND SOLID PHASES

In the extreme quantum limit of $S = 1/2$, there arises the possibility of zero-point quantum fluctuations destroying long-range antiferromagnetic orders when the amplitude of the fluctuations becomes of the order of the spin length. Furthermore, the presence of frustrated interactions enhances quantum fluctuations thereby aiding the stabilization of quantum paramagnetic phases such as quantum spin liquids and valence bond crystals. Here, we investigate the effect of quantum fluctuations beyond the spin-wave approximation by employing resonating valence bond variational wave functions. We first investigate our J_1 - J_2 - J_3 model in parameter regimes where one of the couplings is overwhelmingly stronger compared to the remaining two. In this limiting regime, we note that at zeroth order the strongest bonds will form a singlet or triplet dimer and the locally excited states correspond to singlet to triplet excitations or *vice versa* for antiferromagnetic or ferromagnetic bonds, respectively [see Fig. 10]. The effect of non-zero values of the remaining two (subdominant) couplings is to dynamically create local excitations on the strong singlet and triplet dimer bonds. Hence, an effective Hamiltonian of interacting singlet or triplet bonds between neighboring dimers can be constructed within this approach. This procedure is known to be effective in explaining the low energy physics of interacting spin systems [47–55]. We now discuss the different VBS phases which are found to be realized as variational quantum ground states of the J_1 - J_2 - J_3 model.

A. VBS₁ and VBS₂ phases

In the limit when $|J_1| \gg (|J_2|, |J_3|)$ we have a VBS configuration consisting of dimers on J_1 type bonds [see Fig. 10(a)]. The local Hilbert space is four dimensional spanning the singlet ground state and the three triplets as the excited states. Following Ref. [49], we define $\hat{\psi}_i^\dagger$ and $\hat{\chi}_i^\dagger$ as the creation operators of the singlet and triplet states, respectively, on the i^{th} bond within a given unit cell with the accompanying constraint on the dimensionality of the Hilbert space

$$\hat{\psi}_i^\dagger \hat{\psi}_i + \hat{\chi}_{i,\alpha}^\dagger \hat{\chi}_{i,\alpha} = 2S, \quad (28)$$

where $i = 1$ or 2 corresponds to the two J_1 type of bonds in a unit cell, and $\alpha = 1, 2, 3$ denotes the three types of triplets in a given dimer. The interaction term between the two neighboring unit cells is obtained by writing down the spin components in terms of the above mentioned valence bond operators. This is achieved by calculating $\langle m | \hat{S}_\mu^\nu | n \rangle$ where $\mu = 1, 2$ denotes the two spins in a given dimer, $\nu = x, y, z$ labels the three spin components, and $|m\rangle$ ($|n\rangle$) represents the singlet or triplet states. In general, a spin operator at a given site has the form $\hat{S}_i \approx \frac{1}{2}(\hat{\psi}_i^\dagger \hat{\chi}_i + \text{h.c.})$ where i labels a given dimer [see Appendix B for details]. As a result of this transformation we land up with a Hamiltonian which is quartic in the field operators $\hat{\chi}$ and $\hat{\psi}$. We carry out a mean-field decoupling such that the resulting quadratic Hamiltonian [Eq. (B2)] separates into singlet and triplet sectors with no mixing terms. The ground state energy is obtained by extremizing the Hamiltonian with respect to the mean-field parameter N_i (where $\sqrt{N_i} = \langle \hat{\psi}_i^\dagger \rangle = \langle \hat{\psi}_i \rangle$) and the Lagrange multiplier λ needed to implement the constraint of Eq. (28), which yields two sets of self consistent equations which are solved. The resulting expression for the ground state energy per unit cell for VBS state in the parameter regime $J_1 \gg (J_2, J_3)$ is,

$$\mathcal{E}_a = (N_{a,1} + N_{a,2})E_a - \lambda[(N_{a,1} + N_{a,2}) - 1] + \frac{3}{2N} \sum_{\mathbf{k}} \sum_{i=1}^2 (\Theta_{\mathbf{k},i} - \mathcal{A}_{\mathbf{k},i}), \quad (29)$$

where a labels the VBS₁ state, $\Theta_{\mathbf{k},i}$ is the eigenenergy obtained in the triplon sector of the interacting Hamil-

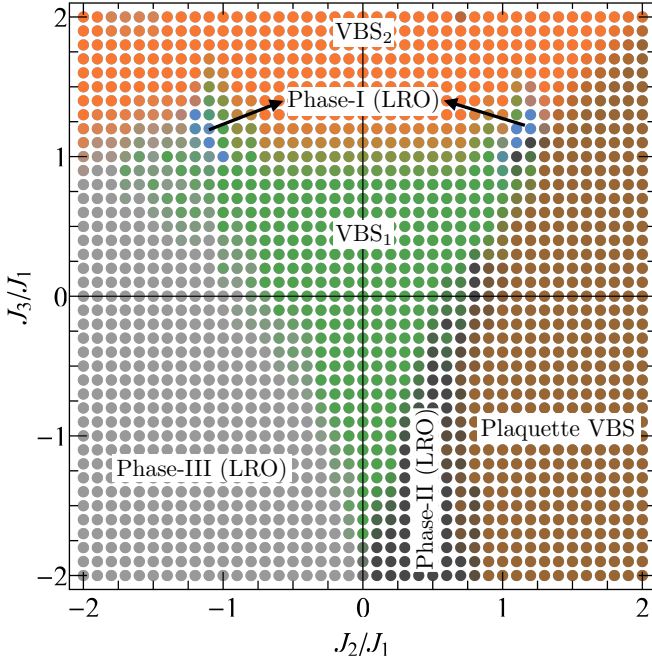


FIG. 11. Quantum phase diagram of the $S = 1/2$ J_1 - J_2 - J_3 Heisenberg model on the Fisher lattice (Fig. 1(a)) obtained by a bond operator analysis. We see the appearance of three different VBS phases in addition to the three long-range ordered (LRO) phases also present in the classical phase diagram (Fig. 2(a)).

tonian Eq. (B2) signifying the excitation of the triplet state [53], and $\mathcal{A}_{k,i}$ is the diagonal element of Eq. (B2). A similar procedure can be followed for the VBS₂ state in the parameter regime $J_3 \gg (J_1, J_2)$. For the VBS₂ state the unit cell has been conveniently chosen as an elementary square. In a similar manner as above, we obtain the ground state energy per square,

$$\mathcal{E}_b = (N_{b,1} + N_{b,2})E_b - \lambda[(N_{b,1} + N_{b,2}) - 1] + \frac{3}{2N} \sum_{\mathbf{k}} \sum_{i=1}^2 (\Pi_{\mathbf{k},i} - \mathcal{B}_{\mathbf{k},i}). \quad (30)$$

where b labels the VBS₂ state, and the remaining terms all have identical meaning to that in Eq. (29) [see Appendix B for further details].

B. Plaquette VBS

In the parameter regime $(J_2, J_3) \gg J_1$ where we expect a plaquette VBS phase [see Fig. 10(c)], we have two choices of forming two dimers inside a square. More precisely, if we denote the four vertices of a square as V_1, V_2, V_3 , and V_4 , then we have two possibilities for dimer formation, namely V_1 - V_2 and V_3 - V_4 or V_1 - V_4 and V_2 - V_3 . The corresponding Hamiltonian is

$$\hat{\mathcal{H}}_p = J_2(\hat{\mathbf{S}}_1 + \hat{\mathbf{S}}_3) \cdot (\hat{\mathbf{S}}_2 + \hat{\mathbf{S}}_4) + J_3(\hat{\mathbf{S}}_1 \cdot \hat{\mathbf{S}}_3 + \hat{\mathbf{S}}_2 \cdot \hat{\mathbf{S}}_4) \quad (31)$$

The diagonalization of the above Hamiltonian gives the following two lowest energy plaquette singlet states,

$$|\Psi_{p,(\pm)}\rangle = \frac{1}{\sqrt{2}}(|\psi_{1,2}\rangle|\psi_{3,4}\rangle \pm |\psi_{1,4}\rangle|\psi_{2,3}\rangle) \quad (32)$$

where $|\psi_{i,j}\rangle$ denotes a singlet state formed between the sites i and j , $|\Psi_{p,+}\rangle$ is the ground state wavefunction with energy $E_+^s = -2J_2 + \frac{J_3}{2}$ and $|\Psi_{p,-}\rangle$ is the first (singlet) excited state with energy $E_{s,-} = -\frac{3}{2}J_3$. Above these states lie the nine triplet states of the plaquette VBS with energies,

$$E_{\mu,\nu}^t = (-J_2 + \frac{J_3}{2})\delta_{\mu,3} - \frac{J_3}{2}(\delta_{\mu,1} + \delta_{\mu,2}) \quad (33)$$

where $\mu, \nu = 1, 2, 3$. The five quintet states have a degenerate energy $E_d = J_2 + \frac{J_3}{2}$. To capture the low-energy dynamics we have restricted our analysis to within the singlet-triplet manifold. The low-energy dynamics now includes, in addition to the triplet excited states considered for the VBS₁ and VBS₂ states, the singlet excited states. Within this approximation the effective low-energy Hamiltonian for a single plaquette can be written as

$$\hat{\mathcal{H}}_p = \sum_{i=\pm} E_{s,i} \hat{\psi}_{p,i}^\dagger \hat{\psi}_{p,i} + \sum_{\mu,\nu=1}^3 E_{t(\mu,\nu)} \hat{\chi}_{(\mu,\nu)}^\dagger \hat{\chi}_{(\mu,\nu)}. \quad (34)$$

The Eqs. (31), (32), and (34) together with the constraint of Eq. (28) provide for a complete description of the low-energy spectrum at zeroth order, i.e., in the absence of a J_1 interaction leading to isolated plaquettes. The presence of a finite J_1 introduces interactions between neighboring plaquettes which induce transitions between different states represented of Eq. (34). The inter-plaquette interactions are obtained by writing the spin components in terms of the above-mentioned plaquette operators as was done for the VBS₁ and VBS₂ states [see Appendix C for details]. The effective low-energy Hamiltonian for the interacting plaquette-VBS state thus obtained is given in Eq. (C3) [see Sec. C for the details]. The ground state energy per plaquette is

$$\mathcal{E}_c = N_{c,+}(E_c - \lambda) + \lambda + \frac{3}{2N} \sum_{\mathbf{k}} \sum_{i=1}^3 (\Omega_{\mathbf{k},i} - \mathcal{C}_{\mathbf{k},i}) \quad (35)$$

where $\sqrt{N_{c,+}} = \langle \hat{\psi}_{p,+}^\dagger \rangle = \langle \hat{\psi}_{p,+} \rangle$, $\Omega_{\mathbf{k},i}$ is eigenenergy obtained in the triplon sector of the interacting plaquette Hamiltonian [Eq.(C3)].

Employing the expressions [Eq. (29), Eq. (30) and Eq. (35)] of the ground state energies of the three phases we map out the resulting phase diagram. The most salient feature of our phase diagram is the appearance of three quantum paramagnetic phases, namely, a plaquette VBS, and two other types of dimer ordered states dubbed VBS₁ and VBS₂ as shown in Fig. 11. The classical region of existence of the uncorrelated AF chain phase is

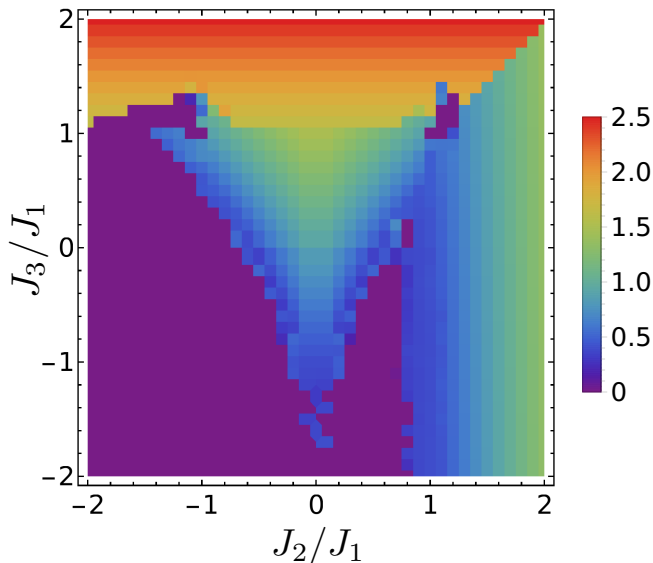


FIG. 12. Density plot of triplet excitation gap obtained by plaquette and bond operator analysis.

now found to be divided into two region under the influence quantum fluctuations. For $J_1 \gg (J_2, J_3)$, the VBS₁ state is stabilized while for $J_3 \gg (J_1, J_2)$, the VBS₂ state is stabilized. At the phase boundary of these two VBS states, a long range order (LRO) state is found to be stabilized in a sliver of parameters space as characterized by the vanishing singlet-triplet excitation gap. We label this long range ordered state as phase-I (LRO) and it is characterized by the ordering vector $Q = (0, k_y), (k_x, 0)$.

Another interesting aspect of the quantum phase diagram is that the Néel phase (labeled as phase-II in Fig. 3) gives was to a plaquette-RVB state irrespective of the sign of the J_3 coupling. On the other hand, the sublattice Néel phase (marked by region-II in Fig. 3) is largely immune to quantum fluctuations, and is referred to as Phase-III (LRO) in Fig. 11. Apart from these phases as described, there is another long range ordered phase found in a small region for negative J_3 and it exists in between VBS₁ and plaquette VBS phases and is labelled as phase-II (LRO) in Fig. 11. The singlet-triplet excitation gap which is used to determine the phase diagram as shown in Fig. 11 is shown as a density plot in Fig. 12.

The above results obtained within bond operator formalism suggests that the large degeneracy in the disordered AFM chain in classical limit may not lead to ground state degeneracy in the exact quantum limit as indicated by the stability of VBS₂ phase with large value of singlet-triplet excitation gap as shown in Fig. 12. On the other hand the Néel phase which is known to be prone under quantum fluctuations is moderately stabilized into plaquette VBS state. It is to be noted that the singlet-triplet excitation gap for VBS₁ state is smaller compared to that of the VBS₂ state. In fact, Fig. 12 suggests that the singlet-triplet excitation gap gradually decreases as value of J_3 decreases. While the uncorrelated AFM chain

phase and Néel phase yield to quantum paramagnetic state under quantum fluctuations, remarkably the sublattice Néel phase is quite stable as evident from Fig. 11. This may be attributed to the fact that the number of nearest neighbour bonds with ferromagnetic alignment is three times than the number of bonds with antiferromagnetic bonds. The other possible explanation is that each square plaquette can be thought of as a large spin with magnitude of $4S$ which protects it from quantum fluctuations. Finally, we note that similar observations of a plaquette VBS, and competing magnetic phases on a variant of the model, namely, the square kagome lattice Heisenberg model, have previously been made [56–61]

VII. DISCUSSION

We have investigated the ground state phase diagram of the Heisenberg model on the Fisher lattice in the presence of first neighbor J_1 , second neighbor J_2 , and third neighbor J_3 Heisenberg couplings, as an attempt to provide a model for magnetism of a two dimensional layer of the Hollandite lattice. At the classical level, a Luttinger-Tisza analysis shows that the phase diagram is host to three different phases, namely, (i) an uncorrelated antiferromagnetic chain phase wherein each horizontal and vertical chain has perfect one-dimensional antiferromagnetic order but the relative orientations between any two chains is not fixed at $T = 0$ [62–64]. This uncorrelated AFM chain phase exists for $J_2 \geq J_3$ and antiferromagnetic J_2, J_3 only. Furthermore, there exist two different Néel phases depending on the sign of J_2 . For antiferromagnetic J_2 , we find a sublattice Néel phase (phase-II) where the four sites within a unit cell are aligned ferromagnetically while such a cluster of ferromagnetic spins forms Néel order. On the other hand for negative values of J_2 we obtain a perfect Néel order (phase-III) where the four spins within a unit cell too are antiferromagnetically ordered.

We have investigated the role of quantum and thermal fluctuations within a harmonic approximation which reveals an order-by-disorder mechanism at play. Firstly, the uncorrelated AFM phase shows a thermal as well as a quantum order-by-disorder transition by selecting a common α for all the one dimensional chains. Though the zeroth order energy in the spin wave approximations are identical for each α , the various details of the spin wave spectrum depend on the choice of α , e.g., the spectrum could be linear or quadratic for specific choices of α , and the number of zero energy modes depends on α . Interestingly the thermal fluctuations lift the degeneracy and selects $\alpha = 0, \pi$ as the preferred ground state configurations. For specific choices of α , the spin-wave spectrum shows Dirac nodal lines along $\bar{\Gamma}\bar{X}$ and $\bar{\Gamma}\bar{Y}$. The spin-wave spectrum for phase-II shows existence of three Dirac nodal loops of which two are symmetry protected and do not depend on the value of J_3 .

Finally, we have employed a bond operator formalism

to analyse the model Hamiltonian beyond the spin-wave wave approximation. The analysis for spin $S = 1/2$ shows that most of the classical phases except the sublattice Néel phase are stabilized into some kind of valence bond states. The uncorrelated AFM phase is stabilized into a VBS₁ dimer order with an appreciable singlet-triplet excitations gap. This VBS₁ phase appears mostly for large positive J_3 . In a triangular shaped region around the centre in $J_2 - J_3$ plane, a VBS₂ dimer state is stabilized. The Néel phase is largely stabilized into a plaquette VBS state, while the sublattice Néel phase is found to be stable under quantum fluctuations within a bond operator formalism.

We expect that our study would set the stage for further investigations into the magnetic phases in the Hollandite lattice [13, 17, 26, 28]. The experimental realization of two dimensional layers of α -MnO₂ (if possible) might serve as a platform to confirm the existence of some of the phases that have been found here. A possible extension of the present study is to include a coupling between such two dimensional layers yielding a three dimensional model of magnetism in Hollandite lattice. As a future endeavor, it would be interesting to study the spin $S = 1/2$ quantum phase diagram employing state-of-the-art numerical quantum many-body frameworks such as pseudofermion functional renormalization group [65] and variational quantum Monte Carlo methods [66] which have already been applied on the square [67] and other two-dimensional lattices. In particular, for $S = 1/2$ the possibility of a quantum spin liquid occupying a region of parameter space cannot be discounted for [68], and it will be worthwhile to carry out a projective symmetry group classification [69] of quantum spin liquids on the Fisher lattice, and analyze their stability and energetic competitiveness with the valence-bond solid orders found in this work.

ACKNOWLEDGEMENTS

Y.I. acknowledges the Science and Engineering Research Board (SERB), DST, India for support through Startup Research Grant No. SRG/2019/000056 and MATRICS Grant No. MTR/2019/001042, and the Abdus Salam International Centre for Theoretical Physics (ICTP) for support through the Simons Associateship scheme. This research was supported in part by the International Centre for Theoretical Sciences (ICTS) during a visit for participating in the program - Novel phases of quantum matter (Code: ICTS/topmatter2019/12) and in the program - "The 2nd Asia Pacific Workshop on Quantum Magnetism" (Code: ICTS/apfm2018/11). This research was supported in part by the National Science Foundation under Grant No. NSF PHY-1748958. The Monte Carlo simulations were performed at SAMKHYA: High Performance Computing Facility provided by Institute of Physics, Bhubaneswar.

Appendix A: Hamiltonian for spin-wave spectrum

In this appendix, we write explicitly the Hamiltonian which is used to find the spectrum of spin wave excitations.

1. Phase-I

For phase-I which we referred as uncorrelated AFM chain phase, the Hamiltonian matrix is,

$$H_{\mathbf{k}} = \begin{bmatrix} A(\mathbf{k}) & B(\mathbf{k}) \\ B(\mathbf{k}) & A(\mathbf{k}) \end{bmatrix}. \quad (\text{A1})$$

The basis vector was chosen as $\hat{\chi}_{\mathbf{k}} = [\hat{\chi}_{\mathbf{k}}, \hat{\chi}_{-\mathbf{k}}^\dagger]^T$, with $\hat{\chi}_{\mathbf{k}} = (\hat{a}_{\mathbf{k},1}, \hat{a}_{\mathbf{k},2}, \hat{a}_{\mathbf{k},3}, \hat{a}_{\mathbf{k},4})$. In the above $A_{\mathbf{k}}$ and $B_{\mathbf{k}}$ is 4×4 matrices which are given below.

$$A_{\mathbf{k}} = \begin{bmatrix} a & b & 0 & -c \\ b & a & -c & 0 \\ 0 & -c & a & b \\ -c & 0 & b & a \end{bmatrix} \quad (\text{A2})$$

$$B_{\mathbf{k}} = \begin{bmatrix} 0 & c & b_x(\mathbf{k}) & -b \\ c & 0 & -b & b_y(\mathbf{k}) \\ b_x^*(\mathbf{k}) & -b & 0 & c \\ -b & b_y^*(\mathbf{k}) & c & 0 \end{bmatrix}. \quad (\text{A3})$$

Among various parameters that appear in the above two equations a, b, c are constants such that $a = \frac{1+J_3}{2}, b = \frac{J_2}{4}(1 - \cos \alpha), c = \frac{J_2}{4}(1 + \cos \alpha)$. $b_{(x/y)}(\mathbf{k})$ is given below,

$$b_x(\mathbf{k}) = -\frac{1}{2}(J_3 + e^{ik_x}), b_y(\mathbf{k}) = -\frac{1}{2}(J_3 + e^{-ik_y}). \quad (\text{A4})$$

2. Phase-II

For the Néel phase, the Hamiltonian becomes a 8×8 hermitian matrix due to four sublattice structure and presence of global antiferromagnetic order. The basis vector which is used to define the Hamiltonian is $\hat{\chi}_{\mathbf{k}} = [\hat{\chi}_{\mathbf{k}}, \hat{\chi}_{-\mathbf{k}}^\dagger]^T$, with $\hat{\chi}_{\mathbf{k}} = (\hat{a}_{\mathbf{k},1}, \hat{a}_{\mathbf{k},2}, \hat{a}_{\mathbf{k},3}, \hat{a}_{\mathbf{k},4}, \hat{b}_{-\mathbf{k},1}^\dagger, \hat{b}_{-\mathbf{k},2}^\dagger, \hat{b}_{-\mathbf{k},3}^\dagger, \hat{b}_{-\mathbf{k},4}^\dagger)$, where $\hat{a}_{\mathbf{k}}$ and $\hat{b}_{\mathbf{k}}$ respectively denotes the up spin and down spin in momentum space. The Hamiltonian is obtained as,

$$H_{\mathbf{k}} = I_{2 \times 2} \otimes \begin{bmatrix} A(\mathbf{k}) & B(\mathbf{k}) \\ B(\mathbf{k}) & A(\mathbf{k}) \end{bmatrix}, \quad (\text{A5})$$

where $A_{\mathbf{k}}$ and $B_{\mathbf{k}}$ are given below.

$$A_{\mathbf{k}} = \begin{bmatrix} d & 0 & -J_3 & 0 \\ 0 & d & 0 & -J_3 \\ -J_3 & 0 & d & 0 \\ 0 & -J_3 & 0 & d \end{bmatrix}, \quad (\text{A6})$$

$$B_{\mathbf{k}} = \begin{bmatrix} 0 & J_2 & e^{ik_x} & J_2 \\ J_2 & 0 & J_2 & e^{ik_x} \\ e^{-ik_x} & J_2 & 0 & J_2 \\ J_2 & e^{-ik_x} & J_2 & 0 \end{bmatrix}. \quad (\text{A7})$$

In the above $d = J_1 + 2J_2 - J_3$ and denote the ground state energy per plaquette in phase-II.

3. Phase-III

For the sublattice Néel phase the basis vector used to define the Hamiltonian matrix for each momentum is identical to phase-II. The Hamiltonian contains few additional parameters. The Hamiltonian has the following expression,

$$H_{\mathbf{k}} = I_{2 \times 2} \otimes \begin{bmatrix} A(\mathbf{k}) & B(\mathbf{k}) \\ B(\mathbf{k}) & A(\mathbf{k}) \end{bmatrix} \quad (\text{A8})$$

where $A_{\mathbf{k}}$ and $B_{\mathbf{k}}$ are given below.

$$A_{\mathbf{k}} = \begin{bmatrix} d & J_2 & -J_3 & J_2 \\ J_2 & d & J_2 & -J_3 \\ -J_3 & J_2 & d & J_2 \\ J_2 & -J_3 & J_2 & d \end{bmatrix}, \quad (\text{A9})$$

$$B_{\mathbf{k}} = \begin{bmatrix} 0 & 0 & e^{ik_x} & 0 \\ 0 & 0 & 0 & e^{ik_x} \\ e^{-ik_x} & 0 & 0 & 0 \\ 0 & e^{-ik_x} & 0 & 0 \end{bmatrix}, \quad (\text{A10})$$

where $d = J_1 - 2J_2 - J_3$ denotes the ground state energy per plaquette in phase-III.

Appendix B: Valance Bond Operator Analysis

In this appendix we provide the detail procedure followed in bond operator formalism. First we give the definition of spins in terms of the fermionic field operator Ψ and χ associated with the singlet and triplet excitations [49, 53] respectively.

$$\hat{S}_{1,\alpha} \approx \frac{1}{2}(\hat{\chi}_{\alpha}^{\dagger} \hat{\psi} + \text{h.c.}), \quad \hat{S}_{2,\alpha} \approx -\frac{1}{2}(\hat{\chi}_{\alpha}^{\dagger} \hat{\psi} + \text{h.c.}) \quad (\text{B1})$$

In the above the subscript 1, 2 refers to two spins within a dimer and $\alpha = x, y, z$ represents the three components of the spin. In defining the above transformation we have restricted upto quadratic powers of the fields. The above definitions can be used to write down the effective Hamiltonian in terms of the field operators. The effective Hamiltonian contains a Lagrangian multiplier λ to satisfy the magnitude of total spin of a given dimer to be $2S$. It is straightforward to observe that the use of Eq. (B1) yields quartic terms in field operators. Mean-field type decomposition has been used to reduce these quartic terms into appropriate quadratic terms in singlet and triplet sector neglecting the mixing between them.

Furthermore as we are interested to find the excitations due to triplets over singlet condensation, we introduce $\sqrt{N_{a,i}} = \langle \hat{\psi}_{a,i}^{\dagger} \rangle = \langle \hat{\psi}_{a,i} \rangle$ as the singlet occupation number which is used to define the zeroth order condensate energy \tilde{E}_a . Here ‘ a ’ denotes the VBS₁ configuration and ‘ $i = 1, 2$ ’ refers to two dimers within an unit cell. Similar definition holds for VBS₂ which can be obtained by replacing the subscript ‘ a ’ by ‘ b ’. With the above discussion and notation, we can write the effective Hamiltonian for the VBS₁ as,

$$\hat{\mathcal{H}}_a = \tilde{E}_a + \frac{1}{2} \sum_{\mathbf{k}} \hat{\phi}_{\mathbf{k},\alpha}^{\dagger} H_{\mathbf{k},a} \hat{\phi}_{\mathbf{k},\alpha}. \quad (\text{B2})$$

In the above the singlet condensate energy \tilde{E}_a is obtained as,

$$\begin{aligned} \tilde{E}_{g,a} &= (N_{a,1} + N_{a,2})E_a^s - \lambda(N_{a,1} + N_{a,2} - 1) \\ &- \frac{3}{2N} \sum_{\mathbf{k}} \sum_{i=1,2} A_{\mathbf{k},a,i} \end{aligned} \quad (\text{B3})$$

where, $A_{\mathbf{k},a,i}$ represents the i^{th} diagonal element of $H_{\mathbf{k},a}$ and $E_a^s = -3J_1/4$ is energy of the singlet states per plaquette. The second term in Eq. (B2) refers to triplet excitations. The basis vector used to obtain Eq. (B2) is $\hat{\phi}_{\mathbf{k},\alpha} = [\hat{\xi}_{\mathbf{k}}, \hat{\xi}_{-\mathbf{k}}^{\dagger}]^T$, with $\hat{\xi}_{\mathbf{k}} = (\hat{\chi}_{a,1,\alpha,\mathbf{k}}, \hat{\chi}_{a,2,\alpha,\mathbf{k}})$, where α denotes different states in triplet sector. It is clear that $H_{\mathbf{k},a}$ is a 4×4 matrix which can be written as,

$$\hat{\mathcal{H}}_{\mathbf{k},a} = \begin{bmatrix} V_{\mathbf{k},a} + D_a & V_{\mathbf{k},a} \\ V_{\mathbf{k},a} & V_{\mathbf{k},a} + D_a \end{bmatrix}, \quad (\text{B4})$$

where V and D are 2×2 matrix given below.

$$V_{\mathbf{k},a} = \begin{bmatrix} -\frac{J_3}{2} N_{a1} \cos 2k_x & J_2 \sin k_x \sin k_y \\ J_2 N_{a12} \sin k_x \sin k_y & -\frac{J_3}{2} N_{a2} \cos 2k_y \end{bmatrix}, \quad (\text{B5})$$

$$D_a = \begin{bmatrix} E_{a,\alpha}^t - \lambda & 0 \\ 0 & E_{a,\alpha}^t - \lambda \end{bmatrix}. \quad (\text{B6})$$

In the above we have used $N_{a,12} = \sqrt{N_{a1} N_{a2}}$. E^t refers to energy of triplet states with $E_{a,\alpha}^t = J_1/4$ i.e all the triplet states are degenerate in energy. To obtain the corresponding representations for VBS₂ we use the singlet and triplet state energy as $E_b^s = -3J_3/4$, $E_{b,\alpha}^t = J_3/4$. All other expressions of $V_{\mathbf{k},a}$ as given in Eq. (B4) will be replaced by $V_{\mathbf{k},b}$ which is given below,

$$V_{\mathbf{k},b} = \begin{bmatrix} -\frac{J_1}{2} N_{b1} \cos k_x & 0 \\ 0 & -\frac{J_1}{2} N_{b2} \cos k_y \end{bmatrix}. \quad (\text{B7})$$

Appendix C: Plaquette Operator Analysis

For the plaquette VBS state represented in Fig. 10(c), the spin operators are obtained as [48],

$$\begin{aligned} \hat{S}_{\delta,\alpha} &\approx c_{\delta,\mu}(\hat{\chi}_{\mu,\alpha}^{\dagger} \hat{\psi}_+ + \text{h.c.}) \\ &+ d_{\delta,\nu}(\hat{\chi}_{\mu,\alpha}^{\dagger} \hat{\psi}_- + \text{h.c.}), \end{aligned} \quad (\text{C1})$$

where $\alpha = x, y, z$, $\mu = 1, 2, 3$ denotes nine triplets and $\delta = 1, 2, 3, 4$ denotes site indices inside a plaquette. A summation over the repeated indices is implied in Eq. (C1). The matrix $c_{\delta,\mu}$ and $d_{\delta,\nu}$ are given below.

$$c_{\delta,\mu} = \frac{1}{\sqrt{6}} \begin{bmatrix} \frac{1}{\sqrt{2}} & 0 & 1 \\ 0 & \frac{1}{\sqrt{2}} & -1 \\ -\frac{1}{\sqrt{2}} & 0 & 1 \\ 0 & -\frac{1}{\sqrt{2}} & -1 \end{bmatrix}, d_{\mu,\nu} = \frac{1}{2} \begin{bmatrix} 0 & 1 & 0 \\ 1 & 0 & 0 \\ 0 & -1 & 0 \\ -1 & 0 & 0 \end{bmatrix} \quad (\text{C2})$$

To derive the effective Hamiltonian as obtained for the valence bond singlet states in Sec. B in Eq. (B2), we follow similar procedure as explained before Eq. (B2). After doing elementary algebra we obtain the effective Hamiltonian in this case as,

$$\hat{\mathcal{H}}_c = \tilde{E}_c + \frac{1}{2} \sum_{\mathbf{k}} \hat{\phi}_{\mathbf{k},\alpha}^\dagger H_{\mathbf{k}} \hat{\phi}_{\mathbf{k},\alpha} + \sum_{\mathbf{k}} (E_-^s - \lambda) \hat{\psi}_{\mathbf{k}-}^\dagger \hat{\psi}_{\mathbf{k}-}. \quad (\text{C3})$$

The first term \tilde{E}_c in the above equation corresponds to ground state condensate energy per plaquette. For the second term, we have used the basis vector as, $\hat{\phi}_{\mathbf{k},\alpha} = [\hat{\xi}_{\mathbf{k}}, \hat{\xi}_{-\mathbf{k}}^\dagger]^T$, with $\hat{\xi}_{\mathbf{k}} = (\hat{\chi}_{1,\alpha,\mathbf{k}} \hat{\chi}_{2,\alpha,\mathbf{k}} \hat{\chi}_{3,\alpha,\mathbf{k}})$. Below we provide explicit expressions of the various terms present in Eq. (C3). First we provide \tilde{E}_t ,

$$\tilde{E}_c = N_{c+} E_+^s - \lambda(N_{c+} - 1) - \frac{3}{2N} \sum_{\mathbf{k}} \sum_{i=1,2,3} \mathcal{C}_{\mathbf{k},i} \quad (\text{C4})$$

where we have used $\sqrt{N_{c+}} = \langle \hat{\psi}_+^\dagger \rangle = \langle \hat{\psi}_+ \rangle$ and λ is the Lagrang multiplier to satisfy the constraint of total angular momentum of the dimer to be $2S$. E_\pm^s is the plaquette singlet state energy for the state $|\Psi_\pm\rangle$ with $E_+^s = -2J_2 + \frac{J_3}{2}$, $E_-^s = -\frac{3J_3}{2}$. $\mathcal{C}_{\mathbf{k},i}$ is the 'i'th diagonal element of $H_{\mathbf{k}}$. The 6×6 hamiltonian matrix($H_{\mathbf{k}}$) in second term in Eq. (C3) is obtained as,

$$\hat{\mathcal{H}}_{\mathbf{k}} = \begin{bmatrix} W_{\mathbf{k}} + D_c & W_{\mathbf{k}} \\ W_{\mathbf{k}} & W_{\mathbf{k}} + D_c \end{bmatrix} \quad (\text{C5})$$

where

$$W_{\mathbf{k}} = \frac{N_{c+}}{3} \begin{bmatrix} -\frac{1}{2} \cos k_x & 0 & \frac{-i}{\sqrt{2}} \sin k_x \\ 0 & -\frac{1}{\sqrt{2}} \cos k_y & \frac{-i}{\sqrt{2}} \sin k_y \\ \frac{i}{\sqrt{2}} \sin k_x & \frac{i}{\sqrt{2}} \sin k_y & \cos k_x + \cos k_y \end{bmatrix} \quad (\text{C6})$$

$$D_c = \begin{bmatrix} E_{1,\alpha}^t - \lambda & 0 & 0 \\ 0 & E_{2,\alpha}^t - \lambda & 0 \\ 0 & 0 & E_{3,\alpha}^t - \lambda \end{bmatrix} \quad (\text{C7})$$

In the above $i, \alpha = 1, 2, 3$ denotes nine triplet states. After diagonalisation the fluctuation due to triplon excitation contributes to the ground state energy and the final expression for the ground state energy can be written as given in Eq. (35). We note that the above analysis has been carried out for $J_2 > J_3$ where $|\Psi_+\rangle$ is the ground state and $|\Psi_-\rangle$ is the first excited states. When $J_3 > J_2$ with $J_1 = 0$, $|\Psi_-\rangle$ becomes the ground state and $|\Psi_+\rangle$ becomes the first excited state. Thus there are parameter regimes where analogous analysis needs to be followed considering $|\Psi_-\rangle$ as the ground state. However after doing that we find that the final energy obtained in the former case i.e when $|\Psi_+\rangle$ is the ground state yields lower energy than the case when $|\Psi_-\rangle$ is the ground state. To obtain the energy expression when $|\Psi_-\rangle$ is the ground state one needs to replace the '-' subscript in the third term in Eq. (C3) by '+', '+' subscript in Eq. (C4) by '-'. The expression of $W_{\mathbf{k}}$ as given in Eq. (C6) have the following form,

$$W'_{\mathbf{k}} = \frac{-N_{c-}}{4} \begin{bmatrix} \cos k_y & 0 & 0 \\ 0 & \cos k_x & 0 \\ 0 & 0 & 0 \end{bmatrix} \quad (\text{C8})$$

-
- [1] W. Heisenberg, "Zur theorie des ferromagnetismus," *Z. Phys.* **49**, 619–636 (1928).
- [2] I. Pomeranchuk, "The thermal conductivity of the paramagnetic dielectrics at low temperatures," *Zh. Eksp. Teor. Fiz.* **11**, 226 (1941).
- [3] Leon Balents, "Spin liquids in frustrated magnets," *Nature* **464**, 199 (2010).
- [4] Lucile Savary and Leon Balents, "Quantum spin liquids: a review," *Rep. Prog. Phys.* **80**, 016502 (2016).
- [5] Yi Zhou, Kazushi Kanoda, and Tai-Kai Ng, "Quantum spin liquid states," *Rev. Mod. Phys.* **89**, 025003 (2017).
- [6] C. Broholm, R. J. Cava, S. A. Kivelson, D. G. Nocera, M. R. Norman, and T. Senthil, "Quantum spin liquids," *Science* **367**, 6475 (2020).
- [7] C. N. R. Rao, "Transition Metal Oxides," *Annu. Rev. Phys. Chem* **40**, 291–326 (1989).
- [8] Sadamichi Maekawa, *Physics of Transition Metal Oxides* (Springer-Verlag Berlin Heidelberg, Germany, 1994).
- [9] Roberto N. DeGuzman, Yan-Fei Shen, Edward J. Neth, Steven L. Suib, Chi-Lin O'Young, Steven Levine, and John M. Newsam, "Synthesis and Characterization of Octahedral Molecular Sieves (OMS-2) Having the Hollandite Structure," *Chem. Mater.* **6**, 815–821 (1994).
- [10] S. Ishiwata, J. W. G. Bos, Q. Huang, and R. J. Cava, "Structure and magnetic properties of hollandite Ba_{1.2}Mn₈O₁₆," *J. Phys. Condens. Matter* **18**, 3745–3752 (2006).
- [11] Kunihiro Hasegawa, Masahiko Isobe, Touru Yamauchi, Hiroaki Ueda, Jun-Ichi Yamaura, Hirotada Gotou, Takehiko Yagi, Hirohiko Sato, and Yutaka Ueda, "Discovery of Ferromagnetic-Half-Metal-to-Insulator Transition in K₂Cr₈O₁₆," *Phys. Rev. Lett.* **103**, 146403 (2009).
- [12] Steven L. Suib and Lennox E. Iton, "Magnetic studies of manganese oxide octahedral molecular sieves: A new

- class of spin glasses,” *Chem. Mater.* **6**, 429–433 (1994).
- [13] Shuangyi Liu, Andrew R. Akbashev, Xiaohao Yang, Xiaohua Liu, Wanlu Li, Lukas Zhao, Xue Li, Alexander Couzis, Myung-Geun Han, Yimei Zhu, Lia Krusin-Elbaum, Jackie Li, Limin Huang, Simon J. L. Billinge, Jonathan E. Spanier, and Stephen O’Brien, “Hollandites as a new class of multiferroics,” *Sci. Rep.* **4**, 6203 (2014).
- [14] Pierre Strobel, Jean Vicat, and Duc Tran Qui, “Thermal and physical properties of hollandite-type $K_{1.3}Mn_8O_{16}$ and $(K,H_3O)_xMn_8O_{16}$,” *J. Solid State Chem.* **55**, 67 – 73 (1984).
- [15] Hirohiko Sato, Jun-Ichi Yamaura, Toshiaki Enoki, and Naoichi Yamamoto, “Magnetism and electron transport phenomena of manganese oxide ion exchanger with tunnel structure,” *J. Alloys Compd.* **262-263**, 443 – 449 (1997), proceedings of the Twelfth International Conference on Solid Compounds of Transition Elements.
- [16] Hirohiko Sato, Toshiaki Enoki, Jun-Ichi Yamaura, and Naoichi Yamamoto, “Charge localization and successive magnetic phase transitions of mixed-valence manganese oxides $K_{1.5}(H_3O)_xMn_8O_{16}$ ($0 < x < 0.5$),” *Phys. Rev. B* **59**, 12836–12841 (1999).
- [17] Y. Crespo, A. Andreanov, and N. Seriani, “Competing antiferromagnetic and spin-glass phases in a hollandite structure,” *Phys. Rev. B* **88**, 014202 (2013).
- [18] Y. Crespo and N. Seriani, “Electronic and magnetic properties of α - MnO_2 from ab initio calculations,” *Phys. Rev. B* **88**, 144428 (2013).
- [19] Naoichi Yamamoto, Tadashi Endo, Masahiko Shimada, and Toshio Takada, “Single Crystal Growth of α - MnO_2 ,” *Jpn. J. Appl. Phys.* **13**, 723–724 (1974).
- [20] Xiong-Fei Shen, Yun-Shuang Ding, Jia Liu, Zhao-Hui Han, Joseph I. Budnick, William A. Hines, and Steven L. Suib, “A Magnetic Route to Measure the Average Oxidation State of Mixed-Valent Manganese in Manganese Oxide Octahedral Molecular Sieves (OMS),” *J. Am. Chem. Soc.* **127**, 6166–6167 (2005).
- [21] J. Luo, H. T. Zhu, F. Zhang, J. K. Liang, G. H. Rao, J. B. Li, and Z. M. Du, “Spin-glasslike behavior of K+-containing α - MnO_2 nanotubes,” *J. Appl. Phys.* **105**, 093925 (2009).
- [22] J. Luo, H. T. Zhu, J. K. Liang, G. H. Rao, J. B. Li, and Z. M. Du, “Tuning Magnetic Properties of α - MnO_2 Nanotubes by K+ Doping,” *J. Phys. Chem. C* **114**, 8782–8786 (2010).
- [23] F. Moussa, M. Hennion, J. Rodriguez-Carvajal, H. Moudden, L. Pinsard, and A. Revcolevschi, “Spin waves in the antiferromagnet perovskite $LaMnO_3$: A neutron-scattering study,” *Phys. Rev. B* **54**, 15149–15155 (1996).
- [24] G. Chaboussant, A. Sieber, S. Ochsenbein, H.-U. Güdel, M. Murrie, A. Honecker, N. Fukushima, and B. Normand, “Exchange interactions and high-energy spin states in Mn_{12} -acetate,” *Phys. Rev. B* **70**, 104422 (2004).
- [25] X. Fabrèges, I. Mirebeau, S. Petit, P. Bonville, and A. A. Belik, “Frustration-driven magnetic order in hexagonal $InMnO_3$,” *Phys. Rev. B* **84**, 054455 (2011).
- [26] S. Mandal, A. Andreanov, Y. Crespo, and N. Seriani, “Incommensurate helical spin ground states on the hollandite lattice,” *Phys. Rev. B* **90**, 104420 (2014).
- [27] M. F. Lapa and C. L. Henley, “Ground States of the Classical Antiferromagnet on the Pyrochlore Lattice,” ArXiv e-prints (2012), [arXiv:1210.6810 \[cond-mat.str-el\]](https://arxiv.org/abs/1210.6810).
- [28] Amber M. Larson, Pouya Moetakef, Karen Gaskell, Craig M. Brown, Graham King, and Efrain E. Rodriguez, “Inducing Ferrimagnetism in Insulating Hollandite $Ba_{1.2}Mn_8O_{16}$,” *Chem. Mater.* **27**, 515–525 (2015).
- [29] J. M. Luttinger and L. Tisza, “Theory of Dipole Interaction in Crystals,” *Phys. Rev.* **70**, 954 (1946).
- [30] J. M. Luttinger, “A Note on the Ground State in Antiferromagnetics,” *Phys. Rev.* **81**, 1015 (1951).
- [31] T. A. Kaplan and N. Menyuk, “Spin Ordering in Three-Dimensional Crystals with Strong Competing Exchange Interactions,” *Philos. Mag.* **87**, 3711 (2007).
- [32] In a Hollandite lattice, the even and odd sublattices lie in different planes, but for the purposes of the present study, this fact is not important.
- [33] In Ref. [17, 26] the J_1 and J_2 couplings in the current paper are labelled as J_2 and J_3 , respectively, while the inter-plane coupling is labelled as J_1 . As we only deal with a given two dimensional plane which is perpendicular to the channel directions, J_1 coupling of earlier studies is absent in our present analysis.
- [34] Kenneth Millard and Harvey S. Leff, “Infinite-Spin Limit of the Quantum Heisenberg Model,” *J. Math. Phys. (N.Y.)* **12**, 1000 (1971).
- [35] Elliott H. Lieb, “The Classical Limit of Quantum Spin Systems,” *Commun. Math. Phys.* **31**, 327 (1973).
- [36] I. Kimchi and A. Vishwanath, “Kitaev-Heisenberg Models for Iridates on the Triangular, Hyperkagome, Kagome, fcc, and Pyrochlore Lattices,” *Phys. Rev. B* **89**, 014414 (2014).
- [37] E.F. Bertaut, “Configurations Magnétiques. Méthode de Fourier,” *J. Phys. Chem. Solids* **21**, 256 – 279 (1961).
- [38] Z. Nussinov, “Commensurate and Incommensurate $O(n)$ Spin Systems: Novel Even-Odd Effects, A Generalized Mermin-Wagner-Coleman Theorem, and Ground States,” ArXiv e-prints (2001), [arXiv:cond-mat/0105253 \[cond-mat.stat-mech\]](https://arxiv.org/abs/cond-mat/0105253).
- [39] S. W. Lovesey, *Theory of Neutron Scattering from Condensed Matter* (A Clarendon Press Publication, Clarendon, Oxford, United Kingdom, 1984).
- [40] J. Villain, R. Bidaux, J.-P. Carton, and R. Conte, “Order as an Effect of Disorder,” *J. Phys. II (France)* **41**, 1263 (1980).
- [41] E. F. Shender, “Antiferromagnetic Garnets with Fluctuationally Interacting Sublattices,” *Zh. Eksp. Teor. Fiz.* **83**, 326 (1982).
- [42] T. Holstein and H. Primakoff, “Field Dependence of the Intrinsic Domain Magnetization of a Ferromagnet,” *Phys. Rev.* **58**, 1098–1113 (1940).
- [43] S A Owerre, “Two-dimensional Dirac nodal loop magnons in collinear antiferromagnets,” *J. Phys. Condens. Matter* **30**, 28LT01 (2018).
- [44] Péter Balla, Yasir Iqbal, and Karlo Penc, “Affine lattice construction of spiral surfaces in frustrated Heisenberg models,” *Phys. Rev. B* **100**, 140402 (2019).
- [45] Christopher L. Henley, “Ordering due to disorder in a frustrated vector antiferromagnet,” *Phys. Rev. Lett.* **62**, 2056–2059 (1989).
- [46] Hikaru Kawamura, “Spin-Wave Analysis of the Antiferromagnetic Plane Rotator Model on the Triangular Lattice—Symmetry Breaking in a Magnetic Field,” *J. Phys. Soc. Jpn.* **53**, 2452–2455 (1984).
- [47] L. O. Manuel, M. I. Micheletti, A. E. Trumper, and H. A. Ceccatto, “Heisenberg model on the $\frac{1}{5}$ -depleted square lattice and the CaV_4O_9 compound,” *Phys. Rev. B* **58**, 8490–8494 (1998).

- [48] R. L. Doretto, “Plaquette valence-bond solid in the square-lattice J_1 - J_2 antiferromagnet Heisenberg model: A bond operator approach,” *Phys. Rev. B* **89**, 104415 (2014).
- [49] Subir Sachdev and R. N. Bhatt, “Bond-operator representation of quantum spins: Mean-field theory of frustrated quantum Heisenberg antiferromagnets,” *Phys. Rev. B* **41**, 9323–9329 (1990).
- [50] Rajiv R. P. Singh, Zheng Weihong, C. J. Hamer, and J. Oitmaa, “Dimer order with striped correlations in the J_1 - J_2 Heisenberg model,” *Phys. Rev. B* **60**, 7278–7283 (1999).
- [51] Valeri N. Kotov, J. Oitmaa, Oleg P. Sushkov, and Zheng Weihong, “Low-energy singlet and triplet excitations in the spin-liquid phase of the two-dimensional J_1 - J_2 model,” *Phys. Rev. B* **60**, 14613–14616 (1999).
- [52] M. E. Zhitomirsky and Kazuo Ueda, “Valence-bond crystal phase of a frustrated spin-1/2 square-lattice antiferromagnet,” *Phys. Rev. B* **54**, 9007–9010 (1996).
- [53] Brijesh Kumar, “Bond operators and triplon analysis for spin- S dimer antiferromagnets,” *Phys. Rev. B* **82**, 054404 (2010).
- [54] Pratyay Ghosh, Akhilesh Kumar Verma, and Brijesh Kumar, “Plaquette-triplon analysis of magnetic disorder and order in a trimerized spin-1 kagome heisenberg antiferromagnet,” *Phys. Rev. B* **93**, 014427 (2016).
- [55] Pratyay Ghosh and Brijesh Kumar, “Spontaneous dimerization and moment formation in the hida model of the spin-1 kagome antiferromagnet,” *Phys. Rev. B* **97**, 014413 (2018).
- [56] Tristan Luga, L. D. C. Jaubert, and Arnaud Ralko, “Topological nematic spin liquid on the square kagome lattice,” *Phys. Rev. Research* **1**, 033147 (2019).
- [57] Hiroki Nakano and Tôru Sakai, “The Two-Dimensional $S=1/2$ Heisenberg Antiferromagnet on the *Shuriken* Lattice –A Lattice Composed of Vertex-Sharing Triangles–,” *J. Phys. Soc. Jpn.* **82**, 083709 (2013).
- [58] Ioannis Rousochatzakis, Roderich Moessner, and Jeroen van den Brink, “Frustrated magnetism and resonating valence bond physics in two-dimensional kagome-like magnets,” *Phys. Rev. B* **88**, 195109 (2013).
- [59] Katsuhiko Morita and Takami Tohyama, “Magnetic Phase Diagrams and Magnetization Plateaus of the Spin-1/2 Antiferromagnetic Heisenberg Model on a Square-Kagome Lattice with Three Nonequivalent Exchange Interactions,” *J. Phys. Soc. Jpn.* **87**, 043704 (2018).
- [60] P. Tomczak, J. Richter, J. Schulenburg and D. Schmalfuß, “Topological nematic spin liquid on the square kagome lattice,” *Condens. Matter Phys.* **12**, 507 (2009).
- [61] Arnaud Ralko and Ioannis Rousochatzakis, “Resonating-Valence-Bond Physics Is Not Always Governed by the Shortest Tunneling Loops,” *Phys. Rev. Lett.* **115**, 167202 (2015).
- [62] P. W. Anderson, “Ordering and Antiferromagnetism in Ferrites,” *Phys. Rev.* **102**, 1008–1013 (1956).
- [63] P. A. McClarty, O. Sikora, R. Moessner, K. Penc, F. Pollmann, and N. Shannon, “Chain-based order and quantum spin liquids in dipolar spin ice,” *Phys. Rev. B* **92**, 094418 (2015).
- [64] Péter Balla, Yasir Iqbal, and Karlo Penc, “Degenerate manifolds, helimagnets, and multi- \mathbf{Q} chiral phases in the classical Heisenberg antiferromagnet on the face-centered-cubic lattice,” arXiv e-prints, arXiv:2007.00376 (2020), arXiv:2007.00376 [cond-mat.str-el].
- [65] Johannes Reuther and Peter Wölfle, “ J_1 - J_2 frustrated two-dimensional heisenberg model: Random phase approximation and functional renormalization group,” *Phys. Rev. B* **81**, 144410 (2010).
- [66] Luca Capriotti, Federico Becca, Alberto Parola, and Sandro Sorella, “Resonating valence bond wave functions for strongly frustrated spin systems,” *Phys. Rev. Lett.* **87**, 097201 (2001).
- [67] Wen-Jun Hu, Federico Becca, Alberto Parola, and Sandro Sorella, “Direct evidence for a gapless Z_2 spin liquid by frustrating Néel antiferromagnetism,” *Phys. Rev. B* **88**, 060402 (2013).
- [68] G. Baskaran, G. Santhosh, and R. Shankar, “Exact quantum spin liquids with fermi surfaces in spin-half models,” (2009), arXiv:0908.1614 [cond-mat.str-el].
- [69] Xiao-Gang Wen, “Quantum orders and symmetric spin liquids,” *Phys. Rev. B* **65**, 165113 (2002).